Soft Matter

Development of coarse-grained molecular dynamics model for poly(dimethyl-co-diphenyl)siloxane

Journal:	*Soft Matter*
Manuscript ID	SM-ART-07-2024-000875.R1
Article Type:	Paper
Date Submitted by the Author:	18-Sep-2024
Complete List of Authors:	Xian, Weikang; University of Wisconsin-Madison, Mechanical Engineering Maiti, Amitesh; Lawrence Livermore National Laboratory, Physical & Life Sciences Saab, Andrew; Lawrence Livermore National Laboratory, Aging and Lifetimes Li, Ying; University of Wisconsin-Madison, Department of Mechanical Engineering

Development of coarse-grained molecular dynamics model for poly(dimethyl-*co*-diphenyl)siloxane

Weikang Xian,[a] Amitesh Maiti,[b] Andrew P. Saab [b] and Ying Li*[a]

a. Department of Mechanical Engineering, University of Wisconsin-Madison, Madison, Wisconsin 53706-1572, USA. E-mail: yli2562@wisc.edu;

b. Lawrence Livermore National Laboratory, Livermore, California 94550 USA

Abstract

Polydimethylsiloxane is an important polymeric material with a wide range of applications. However, environmental effects like low temperature can induce crystallization in the material with resulting changes in its structural and dynamic properties. The incorporation of phenyl-siloxane components, e.g., as in a poly(dimethyl-*co*-diphenyl)siloxane random copolymer is known to suppress such crystallization. Molecular dynamics (MD) simulation can be a powerful tool to understand such effects in atomistic detail. Unfortunately, all-atomistic molecular dynamics (AAMD) is limited both in spatial dimensions and simulation times it can probe. To overcome such constraints and to extend to more useful length- and time-scales we systematically develop a coarse-grained molecular dynamics (CGMD) model for the poly(dimethyl-*co*-diphenyl)siloxane system with bond and non-bonded interactions determined from all-atomistic simulations by the iterative Boltzmann inversion (IBI) method. Additionally, we propose a lever rule that can be useful to generate non-bonded potentials for such systems without reference to all-atomistic ground truth. Our model captures the structural and dynamic properties of the copolymer material with quantitative accuracy, and is useful to study long-time dynamics of highly-entangled systems, sequence-dependent properties, phase behaviour, etc.

Introduction

Polydimethylsiloxane (PDMS) is one of the most widely used silicone materials because of its robust mechanical, thermal, and electrical properties[1,2], which ensures operability over wide temperature range. It also has the advantages of biocompatibility and stability[3,4], and thus used frequently as a matrix, sealant, lubricant, and thermal and electrical insulator in biomedical and aerospace engineering applications.[5–7] However, environmental stimuli like high-dosage radiation exposure, and temperature cycling over wide range can cause significant degradation in the mechanical and other properties of PDMS.[8–12] For example, temperature fluctuations can induce amorphous-to-semi-crystallization transition in PDMS, which can significantly affect its mechanical properties, especially stretchability.[13–15]

Systematic efforts have been made toward improving PDMS's resistance to temperature fluctuations. Chemical and physical cross-linking processes have been used to effectively

enhance elasticity of the materials.[16,17] More importantly, the cross-linking processes create a network structure that can suppress semi-crystallization by forming junctions and very likely, trapped entanglement.[18,19] Incorporation of nanoscale fillers, such as silica nanoparticles, can introduce effective confinement to suppress semi-crystallization as well.[15,20] Copolymerization with other constituents is another strategy to change semi crystallization behaviour of PDMS.[21–24] For instance, siloxane copolymers with phenyl components can maintain rubbery-like hyperelastic properties at low temperatures.[25,26] The incorporation of bulky phenyl side groups along the backbone, e.g. poly(dimethyl-*co*-diphenyl)siloxane (PDMS-*co*-PDPS), significantly changes the microscopic packing of these materials such that crystallization can be greatly impeded.[27–29] It was reported that sufficient suppression of crystalline domain growth can be achieved by incorporating only 3.3 mol% of diphenyl siloxane.[30,31]

Incorporation of substitutional phenyl groups also results in notable changes in the structural and dynamic properties of the silicone materials. There have been experimental studies dedicated to the synthesis of PDMS/PDPS copolymer systems and characterization of their thermal and mechanical properties. For example, Wang and Mark showed that in-situ polymerization of PDPS within crosslinked PDMS matrix yields composites that are much stiffer than the binary blend.[26] On the other hand, viscoelasticity of PDMS-*co*-PDPS copolymer was found to be strongly dependent on the molar ratio of the diphenyl component.[32,33] It is attributed to the fact that the glass transition temperature of the diphenyl component is much higher than the dimethyl counterpart.[27,33–35] However, it remains a challenge to understand the correlation between microstructure and macroscopic mechanical properties of PDMS-*co*-PDPS copolymer. First, accurate quantitative characterization of the copolymer's composition by techniques like nuclear magnetic resonance spectroscopy (NMR) and flourier transformed infrared spectroscopy (FTIR) remains difficult. Such methods only measure overall composition so that microstructures of the material can only inferred at the scale of molecules, giving few information on the sequence of the copolymer.[36–38] Second, techniques like dynamic mechanical analysis (DMA) and differential scanning calorimetry (DSC) only measure thermomechanical properties at the continuum scale,[38] and does not provide a causal link to the underlying microstructure.

Molecular simulations have long been established as an effective tool to investigate microscopic properties of polymeric materials.[39,40] The great advantage of MD simulations lies in the fact that it allows one to probe time-dependent structural and dynamic evolution of model systems explicitly. Such microscopic information is very useful to supplement experimental studies. For example, systematic AAMD simulations by Zhu et al. and by our group provided quantitative insights regarding the diphenyl-dependent structural and dynamic changes of the copolymers.[37,41] We showed that the microscopic packing of the copolymer becomes denser as the molar ratio, represented by ϕ hereafter, of the diphenyl component increases. This is because the phenyl side groups have stronger interactions with each other as compared with interactions between the methyl groups. As a result, the relaxation of the copolymer slows down dramatically, with the relaxation time τ_ϕ increasing approximately as $\tau_\phi \sim \tau_0 10^{2.7\phi}$.[41]

The orders-of-magnitude deceleration in dynamics in PDPS (relative to PDMS) as well as the limited spatial scale that can be simulated at the all-atomistic level (typically up to tens of nm) makes it difficult to investigate long-time relaxation of the copolymer by

AAMD. Therefore, simulation techniques to expand the spatial and temporal scales of MD simulation are extremely important not only in this study but also in other applications. CGMD is one of the effective approaches to overcome the spatial and temporal limitations of AAMD.[42] The essence of CGMD is to reduce the degree-of-freedom (DOF), and thus the computational cost of simulation systems by lumping a few explicit atoms into a CG bead.[43] This not only extends the spatial scales of the simulation but also the time-scale by obviating the need for representing fast internal modes of DOF that are now coarse-grained. However, potential and force must be carefully established for CGMD due to the change of DOF. The development of a CGMD model can be based on either a bottom-up or a top-down approach depending on whether atomistic or macroscopic properties are of interest.[44] An extensive discussion on the topic is beyond scope of this study. Interested readers are referred to a few dedicated reviews in this field.[39,40,42–44]

In this work, we systematically develop a CGMD model for PDMS-*co*-PDPS random copolymer via the IBI method.[44–46] We optimize the CG potential to preserve structural characteristics sampled from AAMD configurations. We propose a lever rule to generate pairwise potential for nonbonded interactions of PDMS-*co*-PDPS with different diphenyl contents. With appropriate time-scaling the derived CG model faithfully captures not only the structural characteristics, but also the dynamic properties of the referential AAMD model. Our model is a promising method to understand the complex behaviour of copolymer materials with computational accuracy and efficiency.

Methods

All-atomistic simulation. AAMD simulation serves as the ground truth based on which our CG model is developed. Details regarding the AAMD simulations can be found in our previous work.[41] Only a brief description is provided here. Copolymer systems were generated by a self-avoiding random walk algorithm, with different molar ratios ϕ of the diphenyl component. The following MD simulations were performed by the Large-scale Atomic/Molecular Massively Parallel Simulator (LAMMPS) package developed by Sandia National Laboratories.[47] The initial structures were first relaxed at T=600 K for 20 ns under *NVT* ensemble to eliminate local features that are in high-energy states. A constant timestep of 0.2 fs was used to ensure numerical stability of these simulations. The systems were then cooled down to T=550 K within periods of 0.2 ns, followed by additional relaxations for 20 ns at the same temperature under *NPT* ensembles at atmospheric pressure. In the final production run, the relaxations were run for up to 300 ns. Results of mean-squared displacement and internal end-to-end distances were used to confirm the full relaxation of all the simulation systems.[41] Results of simulations from the previous work, with ϕ=0, 0.2, 0.4, and 0.6, were used in the current study. Each of these systems employed N_c=100 linear chains, each chain consisting of N=50 monomers with a fraction ϕ of dimethyl groups randomly substituted by diphenyl groups. In addition, we followed the same protocol to generate systems with ϕ=0.05, 0.1, and 0.15, but with N_c=90 chains and N=40 monomers. A system with ϕ=1.0 (i.e., PDPS) was also generated for the sake of validation of our CG mapping, as will be shown in a following section. A summary of the AAMD simulations is provided in Table 1. For ϕ=0.4, a portion of an individual chain is shown in Fig. 1(a), and the whole simulation system is shown in Fig. 1(b) with hydrogens not displayed for visualization clarity. All visualizations were done using the Visual Molecular Dynamics (VMD) package.[48]

Iterative Boltzmann inversion. In our CG model, one bead was used to represent one atomistic dimethyl or diphenyl monomer. Positions of the backbone silicon atoms were chosen to be the centres of the CG beads because such a choice simplifies bond, angle, and dihedral definitions at the CG level.[49] CG bead type CGB1 and CGB2 were labelled for the dimethyl and diphenyl monomers, respectively. The mapping scheme is shown in Fig. 1(c). For comparison with the atomistic counterparts, the same copolymer molecule is shown in CG representation in Fig. 1(d) while the whole CG system is shown in Fig. 1(e).

Potentials for bonded and non-boned interactions were optimized by the IBI method. Structural distributions collected from the ground truth AA simulations were used as targets for the optimization. Initial guess of the potentials was generated by direct Boltzmann inversion, as given in Eq. 1, where U, P, and q respectively stand for potential, probability of distribution (obtained using appropriate histogram from MD trajectory analysis), and interaction coordination(s), and k_B and T are the Boltzmann constant and absolute temperature, respectively.

$$U(q) = -k_B T \ln P(q) \qquad \text{Equation (1)}$$

Bonded interactions include bond-stretching, angle, and dihedral interactions with l, θ, and Φ being the respective coordinates. Non-bonded interactions are the pair-wise interactions between beads that are not directly bonded, with r being the inter-bead distance coordinate. Considering two different bead types in the copolymer system, a total of three, six, ten, and three different types of potentials are necessary in the CG model to represent CG-level bond, angle, dihedral, and pair interactions, respectively. A detailed list of the labels is presented in Table S1. It is worth noting that the distributions of bonded interactions do not change significantly as ϕ varies from 0 to 0.6, as shown in Figs. S1, S2, and S3. Therefore, we assumed that the distributions of bonded interactions are independent of ϕ and thus calculated the target distributions by averaging AA distributions of all systems with different ϕ. The IBI optimization was performed by a hybrid protocol combining an in-house MATLAB code and the open-sourced package Versatile Object-oriented Toolkit for Coarse-graining Applications (VOTCA).[50] The optimization proceeds in an iterative fashion as given by Eq. 2, where $U^{(n)}$and $P^{(n)}$are the current potential and distribution, respectively. P^{target} is the target AA ground truth. λ is a linear coefficient that controls the strength of perturbation. λ=0.05 was used in all optimization processes.

$$U^{(n+1)} = U^{(n)} + \lambda k_B T \ln(P^{(n)}/P^{\text{target}}) \qquad \text{Equation (2)}$$

Non-bonded interactions. Unfortunately, distributions of pair interactions are dependent on ϕ, such that the pair interactions optimized for one system are generally not applicable to a system with different ϕ. This is known as the *transferability* issue, to which generic solutions remain a challenge.[43] We devised a practical solution to this problem specifically as it relates to the copolymer systems studied in this work. First, we optimized pair potentials for systems with ϕ=0, 0.2, 0.4, and 0.6. Pressure corrections were applied to refine the IBI derived pair potentials to preserve the target AA densities in CG simulations. Then, instead of direct IBI optimization, pair potentials for ϕ=0.05, 0.1, 0.15 systems were derived based on the IBI-optimized results for ϕ=0, 0.2, and 0.4 systems. Each of the pair potentials $U_{\phi}^{(x)}$ was derived according to the lever rule given in Eq. 3,

where $U_{\phi_1}^{(x)}$ and $U_{\phi_2}^{(x)}$ are two ends of the lever and superscript *x* stands for the label of the pair interaction (*x*=1, 2, 3).

$$U_{\phi}^{(x)} = \frac{\phi_2 - \phi}{\phi_2 - \phi_1} U_{\phi_1}^{(x)} + \frac{\phi - \phi_1}{\phi_2 - \phi_1} U_{\phi_2}^{(x)} \qquad \text{Equation (3)}$$

In the derivation of the unknown pair potential associated with a given ϕ, two already known pair potentials (from IBI) were chosen from ϕ=0, 0.2, and 0.4 to calculate the two corresponding lever ends. The desired pair potential $U_{\phi}^{(x)}$ was then generated according to Eq. 3. Specifically, since pair.1 interaction (CGB1---CGB1) was available for pure PDMS (i.e., ϕ=0.0), the IBI-based potential for ϕ=0 and 0.2 were used as levers to linearly interpolate the pair.1 interaction for small ϕ. For instance, $U_{\phi=0.05}^{(1)} = 0.75U_{\phi=0}^{(1)} + 0.25U_{\phi=0.2}^{(1)}$, and $U_{\phi=0.1}^{(1)} = 0.5U_{\phi=0}^{(1)} + 0.5U_{\phi=0.2}^{(1)}$. However, since pair.2 (CGB1---CGB2) and pair.3 (CGB2---CGB2) interactions were not available for pure PDMS, we employed ϕ=0.2 and 0.4 as levers to estimate such interactions. For instance, $U_{\phi=0.1}^{(2)} = 1.5U_{\phi=0.2}^{(2)} - 0.5U_{\phi=0.4}^{(2)}$, which is an extrapolation.

Dynamics. Dynamics of the CG model is expected to be faster than the AA ground truth because of the decrease in DOF. To quantify the AA-to-CG acceleration, mean-squared displacements of the chain molecules from AA and CG simulations were examined. Diffusive motion of the centre-of-mass (CM), $g_3(t)$, of the chain molecules were calculated according to Eq. (4), where $\boldsymbol{R}_{\mathrm{CM}}$ and angular parenthesis represent the CM of individual chains and ensemble average respectively.

$$g_3(t) = \langle [\boldsymbol{R}_{\mathrm{CM}}(t) - \boldsymbol{R}_{\mathrm{CM}}(0)]^2 \rangle \qquad \text{Equation (4)}$$

Diffusion coefficients $D_{\mathrm{c}} = g_3/6t$ were calculated for AA and CG systems respectively to recalibrate the accelerated dynamics. The rescaling factors S_τ were then calculated by $S_\tau = D_{\mathrm{c,CG}}/D_{\mathrm{c,AA}}$, such that CG dynamics were remapped back into AA space.[46] For long-chain cases where entanglement (topological uncrossability between chains) significantly changes the overall molecular relaxation, *Z1* analyses were applied to quantify the entangled structures and corresponding time-dependent evolutions.[51–53] The *Z1* algorithm identifies entanglement points, i.e. *kinks*, formed by the primitive paths of different chains, and thus can estimate the number of these points, $\langle Z \rangle$, via averaging over MD trajectories. In the tube theory of entangled melts the topological uncrossability is interpreted as constraining the dynamics of chain segments within tubular regions of an average radius a_{pp}, which is a quantification of the strength of the constraint.[54–56] The quantity a_{pp} and related structural characteristics such as chain-length between entanglement points, $N_{\mathrm{e}}^{\mathrm{ck}}$, can be computed by *Z1* analysis. In addition, one-dimensional diffusion (reptation) within the tube-like region can be monitored by the tube survival probability function $\psi(s,t)$ that describes the probability of certain chain segment, s, moves out from the original tube-like region at time t.[57,58]

Initial CG Configurations and Equilibration. Initial CG trajectories were generated based on the respective equilibrated AA trajectories if they are available. On the other hand, for systems without available AA references, the CG trajectories were generated by a two-step protocol. First, monomer sequences were assigned to the linear chains according to the

given ϕ, which was followed by the generation of self-avoiding random-walk trajectories without enforcing any characteristic distributions of the angle, dihedral and pair interactions. Such initial conformations, as one would expect, have structural statistics very different form the target distributions. In the second step, an in-house protocol based on LAMMPS scripting was used to initially equilibrate the random-walk trajectories. Full potentials of the bond, angle, and dihedral interactions were directly applied. But the strengths of the pair interactions were gradually turned on via a linear coefficient, that was increased from 0 to 1.0, with increments in steps of 0.01. Within each step of the linear coefficient the bond length and system temperature were monitored. Once the fluctuations of the bond length and system temperature were both within 5% of the target values the linear coefficient was incremented to the next level. Such stepwise protocol is very similar to the soft-repulsion protocols that have been well established.[59] Additional relaxations that lasted for 10 to 100 ns were applied to the derived trajectories under *NPT* ensemble to ensure convergence in densities. Degree of polymerization, N, for all ϕ, ranged from 40 to 800.

To justify our mapping scheme of coarse-graining a whole dimethyl or a diphenyl group into a single CG bead, an extra mapping scheme for pure PDPS was also developed in which two addition side beads were defined at the geometric centres of the phenyl rings of the side groups for an individual chemical monomer, as shown in Fig. S4 (a) and (b). The backbone CG beads were defined in the same way as in the first mapping scheme. The corresponding snapshot of a chain molecule for the AA and the two CG schemes are shown in Fig. S4. With the additional beads, additional interactions and thus extra potential terms were needed. Optimized CG potential for this alternative mapping scheme and the first scheme (described above) were used to run short simulations. The structural distributions for the alternative and the first schemes were collected form the short runs. The results are shown in Figure S5 to S8, and S9, respectively. As shown in Fig. S10, both mapping schemes capture the AA ground truth very well in terms of the probability distributions of mean-squared end-to-end distance and mean-squared radius of gyration. However, the first scheme is more coarse-grained, and thus simpler because it requires less interaction types to be defined and optimized, and thus computationally more efficient as well. Therefore, we adopted the first mapping in all the other simulations.

Results

All CG simulations were performed on Lassen cluster with NVIDIA V100 GPU in Livermore Computing Centre of Lawrence Livermore National Laboratory. A fixed timestep of 5 fs was employed. The CG model was found to yield several orders-of-magnitude gain in computational speed. For example, the CG model with N_c=800 chains and chain-length N=50 for pure PDMS (ϕ=0) took about 10 minutes to run a simulation of length of 30 ns (rescaled), while it took 60 hours to run an AA model of pure PDMS with N_c =100 chains and N=50 on an equivalent hardware (40 IBM Power 9 CPU cores with 4 GPUs).

We found that the direct-bond potentials can be well-represented by harmonic potentials since the distributions are Gaussian. Bond distributions that are sampled from the optimized CG model are shown in Fig. 2. The CG bond potentials capture the Gaussian distributions of the target AA ground truth with excellent accuracy. The locations of peaks in the distributions are at about 0.32 nm for all three bond types. However, the harmonic spring

constants are 1.81×10^4, 1.85×10^4, and 1.99×10^4 kcal/mol/nm^2 for bond.1, bond.2, and bond.3 respectively. For angle, dihedral, and pair potentials, tabulated forms were used instead of explicit formula. The CG angle distributions are compared with the target AA ground truth as shown in Fig. 3. They cannot be described by single-mode Gaussian functions. The locations of peaks also differ for the different angle types. The CG dihedral distributions are compared with the target AA ground truth in Fig. 4. It is worth noting that only minor deviations from the target AA ground truth are observed for dihedral.4 and dihedral.9 of ϕ=0.2 system and dihedral.10 of ϕ=0.4 system. The minor deviations are attributed to possible insufficient statistics because those interaction types are low in frequency. We would like to emphasize that the same set of bond, angle, and dihedral potentials were used in all simulations regardless of ϕ because of the ϕ-independent assumption mentioned above. The ϕ-dependent radial distribution functions (RDFs) are shown in Fig. 5. The first peaks for all types shift rightward as ϕ increases, which is consistent with our previous work.[41] The pressure-corrected pair potentials sufficiently capture the target AA RDFs. It is worth noting that our CG model automatically preserves the chain-uncrossability behaviour and there was no need to include extra potentials to enforce such uncrossability as in previous work.[60]

For systems with ϕ=0.05, 0.1, 0.15, we generated the pair potentials using the lever rule (Eq. (3)). Below we refer to such interpolated/extrapolated pair potentials as 'synthetic' potentials (as opposed to IBI-optimized potentials utilizing AA ground truth). Fig. 6(a-c) plot the synthetic pair potentials for systems of ϕ=0.05, 0.1, 0.15, in comparison with potentials for ϕ=0, 0.2. The potential curves were shifted vertically for visual clarity in the main panels. But there is no shift in the insets for direct comparison. As expected, the potentials show smooth transition from ϕ=0 to 0.2 because of the linear interpolation/extrapolation. It is worth noting that amplitudes of the potentials elevate as ϕ increases, which is shown by the insets of Fig. 6(a-c). Such transition agrees with the fact that the inter-bead separations increase with ϕ, as we found in our previous study.[41] To validate the synthetic potentials, equilibrium CG simulations were conducted using the synthetic pair potentials, from which RDFs were sampled. Fig. 7 shows the comparison between the CG RDFs and the AA counterparts, where symbols and solid lines represent the CG and AA results, respectively. The CG pair potentials well capture the referential RDFs despite insignificant differences around the peaks. The differences of pair.3 are anticipated to be the largest because of the insufficient statistic mentioned above. Distributions of bond, angle, and dihedral interactions for systems of ϕ=0.05, 0.1, 0.15 are provided in from Figs. S11 to S13. The consistence between the sampled and the target distributions shows that the bonded interactions are indeed independent of ϕ. We also calculated the overall structure factors for CG and AA simulations to further confirm the local packing of the polymer chains, as presented in Fig. S14. The rightward shifts in the RDFs are more clearly demonstrated by the leftward shifts of local peaks from about 6 nm^{-1} to 8 nm^{-1} in the reciprocal space, in both the AA and CG results. It is to be noted that the ϕ-independent bonded potential may be a special case in modelling copolymer. Copolymer or block copolymer with strongly incompatible constituents may not show such independence. Although our choice is based on the observed ϕ-independence, we hypothesize that the lever rule can also be applied to generate the bonded potentials. However, it is expected that both ends of the lever rule will be very similar to each other,

i.e., $U_{\phi_1}^{(x)} \sim U_{\phi_1}^{(x)}$, when the lever rule is applied. Therefore, the generated potentials will degenerate to the ϕ-independent potentials we used here.

In addition to the local structural distributions, the CG potentials, especially the synthetic ones, also preserve the overall AA density as shown in Fig. 8. The increases in density are as expected as chain-length N increases. When N is fixed, the density increases as a function of the value of ϕ, which in good agreement with our previous study based on AA results.[41] In Fig.8, edged smaller symbols are for CG results, and unedged larger symbols are for the corresponding AA ground truth. The CG density values are consistent with the AA counterparts despite minor differences. The synthetic pair potentials perform surprisingly well since no intended pressure correction was applied to the synthetic potentials.

We investigated the molecular structures in detail as well. In Fig. 9(a) and (b), distributions of the mean-squared end-to-end distance, $\langle {R_{\mathrm{ee}}}^2 \rangle$, and the mean-squared radius of gyration, $\langle {R_{\mathrm{g}}}^2 \rangle$, are shown for all systems. All results were sampled from N=100 simulations and were normalized. As ϕ increases, the peaks shift rightward, because the average size of individual molecules is larger with the increased value of ϕ. Overall, the molecules are in the shape of a prolate ellipsoid, whose aspect ratio increases as a function of ϕ, as indicated by Fig. 9(c) and by eigenvalues of the gyration tensor shown in Fig. S15. These observations are in line with our previous AAMD study.[41] Chain stiffness was also calculated based on the mean-squared internal distance, as shown in Fig. S16. The increase in aspect ratio is attributed to the increased chain stiffness.

We used the *Z1* algorithm to quantify the entangled structure of long-chain cases.[53] The results are shown in Fig. 10. Chains shorter than N=100 showed no entanglement as values of the average $\langle Z \rangle$ are smaller than unity. We restrict the investigations to systems with N up to 400 since systems with longer chains (N=600 and 800) require an extremely long time to equilibrate and to provide fully relaxed results. Fig. 10(a) plots the entanglement number (i.e., the average number of entanglements per chain) as a function is plotted as a function of N for different values of ϕ. Linear correlations with N are observed in all cases. For fixed N, $\langle Z \rangle$ increases slightly with ϕ. Such behaviour is expected because of the increase in chain stiffness. The same trends are also true for ϕ=0.05, 0.1, 0.15, although we do not include these results for visual clarity. Similar trends for primitive path length L_{pp} are observed in Fig. 10(b). While the N-dependence of L_{pp} is expected due to the increase in $\langle Z \rangle$ with increasing N, the ϕ-dependence is strongly correlated to the increase in chain stiffness and aspect ratio. In Fig. 10(c) the average tube diameter, a_{pp}, display sub-linear N-dependence, with saturating behaviour at N~400 for small values of ϕ. The ϕ-dependence of a_{pp}, however, indicates that the effective constraint weakens as ϕ increases. Finally, the entanglement length $N_{\mathrm{e}}^{\mathrm{ck}}$, i.e., the average number of monomers between entanglement points increases as a function of N, due to the unentangled-weakly entangled state transition, as in Fig. 10(d). It is worth noting that all the entanglement structural characteristic are plotted as functions of N in the main manuscript, while additional plots as functions of ϕ are also provided in Fig. S17. We prospect that the entanglement characteristics would converge when values of N are sufficiently large. Experimentally, the tube diameter and the entanglement molecular weight were determined to be a_{pp}=7.3 nm and M_{e}=9.6 kDa, respectively.[61] This entanglement molecular weight corresponds to $N_{\mathrm{e}}^{\mathrm{rheo}}$ =129.9. An investigation by Everaers shows that $N_{\mathrm{e}}^{\mathrm{rheo}} \approx 2N_{\mathrm{e}}^{\mathrm{topo}}$, where $N_{\mathrm{e}}^{\mathrm{topo}}$ is the

topological estimation based on algorithms like *Z1*.[62] The values of a_{pp} and $N_{\mathrm{e}}^{\mathrm{ck}}$, calculated from the PDMS system with N=400, are 6.9 nm and 67.1, respectively. The value of $2N_{\mathrm{e}}^{\mathrm{ck}}$ =134.2 is in a good agreement with the experimental $N_{\mathrm{e}}^{\mathrm{rheo}}$. The discrepancy between the simulation and experimental results is attributed to the fact that the entanglement is not fully developed with limited N, preventing convergence in the characteristic values of the entanglement structure.[63] Additionally, the temperature used in the simulation is much higher than the experimental value, which may cause changes in the structural characteristics of the entanglement system. It is worth noting that the result of experimental characterization of the entanglement structure for PDPS is not available because of its high transition temperatures, which lead to difficulties in synthesis and characterization.[64] More detailed investigations on structure and dynamics of the entangled state will be future work.

Results of the time-rescaling factor S_τ as a function of ϕ are presented in Fig. 11(a). The observed monotonic increase is expected because the coarse-graining level in the CG model increases with ϕ, as one CGB2 bead lumps twenty-four atoms while one CGB1 bead lumps only ten atoms. The CG dynamics were remapped to the AA space with the rescaling factors, S_τ, as shown in Fig. 11(b) for the diffusion coefficients D_{c} as functions of N. The diffusion coefficient characterizes the motion of the chains. The transparent blue and green regions mark the unentangled and weakly entangled systems respectively. The dashed lines represent the scaling law power according to the Doi-Edwards tube model. The N-dependence displays powers of about -1.5 and -1.8 for the unentangled and the weakly entangled regime, respectively. The dependence is not in line with either the Rouse model (-1.0) or the Doi-Edwards tube model (-2.0).[55] This discrepancy suggests that the values of N are insufficient to capture fully entangled characteristics of the copolymer systems. On the other hand, the ϕ-dependence shown in Fig. 11(c) is consistent with our previous AA study that reports a power of -2.7.[41] The dynamics slowdown can be attributed to the increase in the average monomeric friction coefficient as interaction between the diphenyl groups are much stronger than that between the dimethyl groups.

To further quantify the local motion at the segmental scale, we also analysed time-dependent tube survival probability for all entangled systems. Some of these results are shown in Fig. 12, illustrating the effects of N and ϕ on the probability $\psi(s,t)$. Values of natural curvilinear coordinate s are represented by different colours. Only results for 0 to 0.5 are shown because of the expected symmetry between s=0 to 0.5 and s=0.5 to 1.0. All presented results are rescaled with the rescaling factors accordingly. In the cases of N=100 and ϕ=0, 0.4, and 0.6, i.e. Fig. 12(a-c), ψ decays sufficiently and approaches 0 as the chains move out of the original tubes, i.e., full relaxations occur within simulation time. Increasing ϕ strongly decelerates the relaxation, as expected. Similar trends are observed in the cases of N=250 and ϕ=0, 0.4, and 0.6, i.e. Fig. 12(d-f). The level of deceleration increases significantly, as shown in Fig. 12(g-i). In the cases of N=400 and ϕ=0, 0.4, and 0.6, all ψ curves barely converge. But full relaxations are still assumed, because: (1) the scaling of -2.7 shown in Fig. 11(c) holds in the cases of N=400 and (2) tube diameter a_{pp} increases, as shown in Fig. 10(c), which may increase the threshold values of ψ to identify chain escape from the original tube region.

Discussion. Within the scope of this work, both ϕ-dependence of the structural and dynamic properties of PDMS-*co*-PDPS copolymers are well captured. It will be important to investigate longer-chain systems to probe fully entangled characteristics of the copolymer systems. As mentioned, AAMD is usually limited by its accessible spatial and

temporal scales while highly coarse-grained CGMD may require artificial interactions to capture correct structural and dynamic properties.[65–67] Application of our CGMD model to investigate fully entangled systems will bridge the previous AAMD to future mesoscale simulations, which facilitates a multiscale computational framework that links atomistic microstructure to mesoscale relaxation of the bulk materials.[45,60]

Although we focus on PDMS-*co*-PDPS random copolymer here, our model can be used to investigate block copolymers. Our previous AAMD simulation and other experimental studies showed that the glass transition temperature of the diphenyl component is much higher than that of the dimethyl component.[26,27,41] This mismatch can lead to incompatibility between the two constituents and thus possibly induce microscopic phase separation, which can be likely used to design materials with superior mechanical properties.[65–67] The proposed interpolation/extrapolation method for the non-bonded interaction shows advantageous transferability in terms of the ϕ-dependence, although we acknowledge that the method does not guarantee transferability in other thermodynamic conditions like temperature and pressure. However, its application to the understanding of interesting phase behaviour[68,69] at the given temperature and pressure of the copolymer systems is straightforward. Generally speaking, temperature and pressure transferability can be achieved by refining the pairwise interactions in a top-down fashion to match the thermodynamic states and/or properties of interest, like Young's modulus and the Flory-Huggins parameter. For example, energy renormalization is an approach that remaps the LJ parameters to enable the CG model to reproduce Young's modulus of the polymer material in the bulk.[70] On the other hand, regarding compositional transferability, one may observe ϕ-independence in other systems with different polymer components. For example, in a recent work studying copolymer of polystyrene (PS) and poly(methyl methacrylate) (PMMA), ϕ-independence is also observed.[71] Although there is no rigorous theoretical support can be provided, the assumption of ϕ-independent bonded potentials is of great practical advantage.

Additionally, our CG model can be useful to investigate and design copolymer systems in terms of sequence-dependent properties. Synthesis of polymers with precisely controllable sequences has been developed in the past two decades.[72,73] However, it remains a challenge to establish a predictive framework to guide the design of polymers according to desired properties. Recently, data-driven and machine-learning techniques haves attracted considerable attention.[74,75] The generation of training data by molecular (dynamics) simulations relies on capable potentials. We believe that the lever rule proposed in the current work is applicable to other copolymer systems as well, which can enable efficient database generation for data-driven studies.

Conclusions

The ratio between the dimethyl and diphenyl components, quantified by ϕ, dictates the structural and dynamic properties of the PDMS-*co*-PDPS random copolymer. A systematic CG model is proposed in this current work for PDMS-*co*-PDPS with different ϕ values. Our CG model is derived by the IBI optimization based on referential AA simulations as the ground truth. The potentials of bonded and non-bonded interactions are derived iteratively. In addition, the interpolation/extrapolation method is used to derive non-bonded interactions for systems that lacks AA simulation reference. Our CG model shows good capabilities in capturing the structural and dynamic properties of the copolymers.

Particularly, it predicts the molecular relaxation of the copolymers well, which is important in understanding the viscoelasticity of the copolymer materials for various applications.

Author Contributions

Weikang Xian: computational implementation, data analysis, conceptualization, methodology and original draft writing. Amitesh Maiti: supervision and draft revision. Andrew P. Saab: supervision and draft revision. Ying Li: computational implementation, conceptualization, resources, supervision, project administration, funding acquisition, and draft editing.

Conflicts of interest

There are no conflicts to declare.

Acknowledgments

The work at LLNL was performed under the auspices of the U.S. Department of Energy by Lawrence Livermore National Laboratory under contract DE-AC52-07NA27344. Y. L. also would like to thank the support from the National Science Foundation (CMMI-2314424, CMMI-2316200, CAREER-2323108). We also would like to thank the helpful discussions with Prof. Martin Kröger (ETH Zurich) about the Z1 algorithm and generation of equilibrium polymer configurations.

Table 1. Summary of parameters of the AAMD simulations as ground truth in the current work. Results of systems with ϕ =0, 0.2, 0.4, 0.6 and 1.0 were from our previous work.[41]

ϕ	0	0.05	0.1	0.15	0.2	0.4	0.6	1.0
N_c	100	90	90	90	100	100	100	100
N	50	40	40	40	50	50	50	50

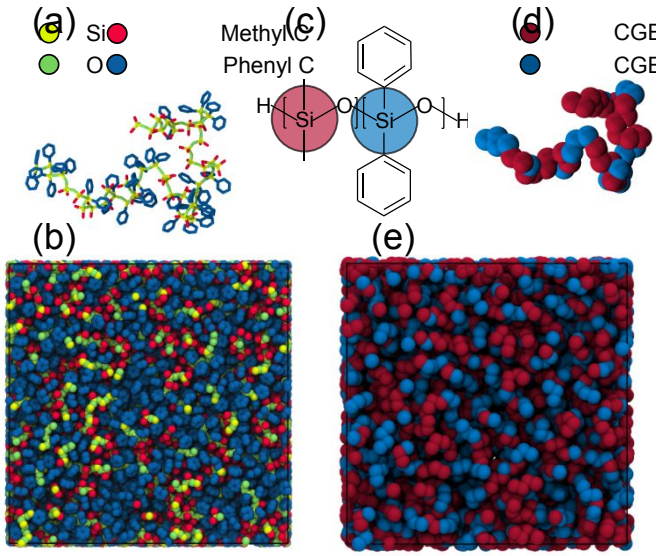

Figure 1. Simulation setup. (a) a single chain and (b) the whole simulation system in AA representation for ϕ=0.4 without displaying any hydrogen atom for visual clarity. (c) CG mapping scheme. The backbone silicon atoms picked as the centres of the CG beads picked. (d) and (e) are the CG representations corresponding to (a) and (b) respectively.

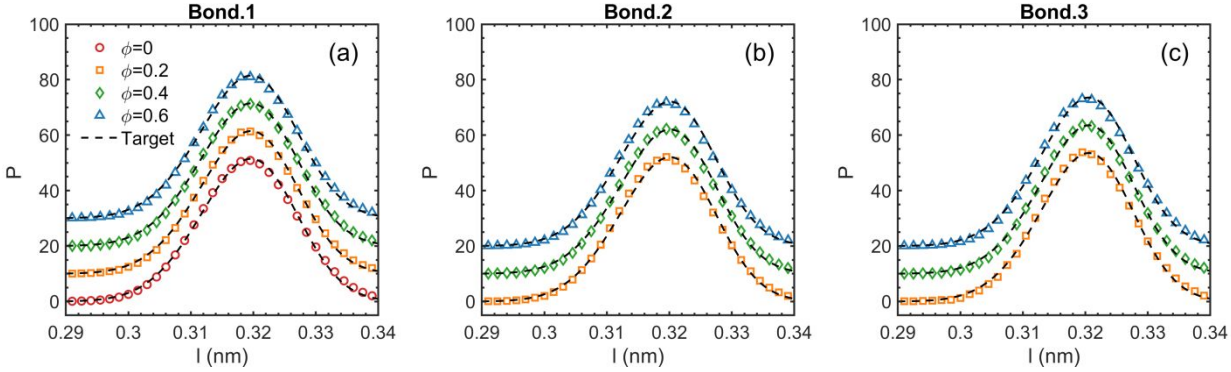

Figure 2. Bond distributions from simulations using the optimized CG model. (a), (b), and (c) are for bond.1, bond.2, and bond.3, respectively. The dashed black lines are the AA target distribution, based on which CG bond potentials were optimized. Vertical shifts are applied for visual clarity. When ϕ=0, there are no bond.2 and bond.3 types of interactions. All distributions can be fitted with single mode gaussian functions such that CG bond potentials can be represented by harmonic functions.

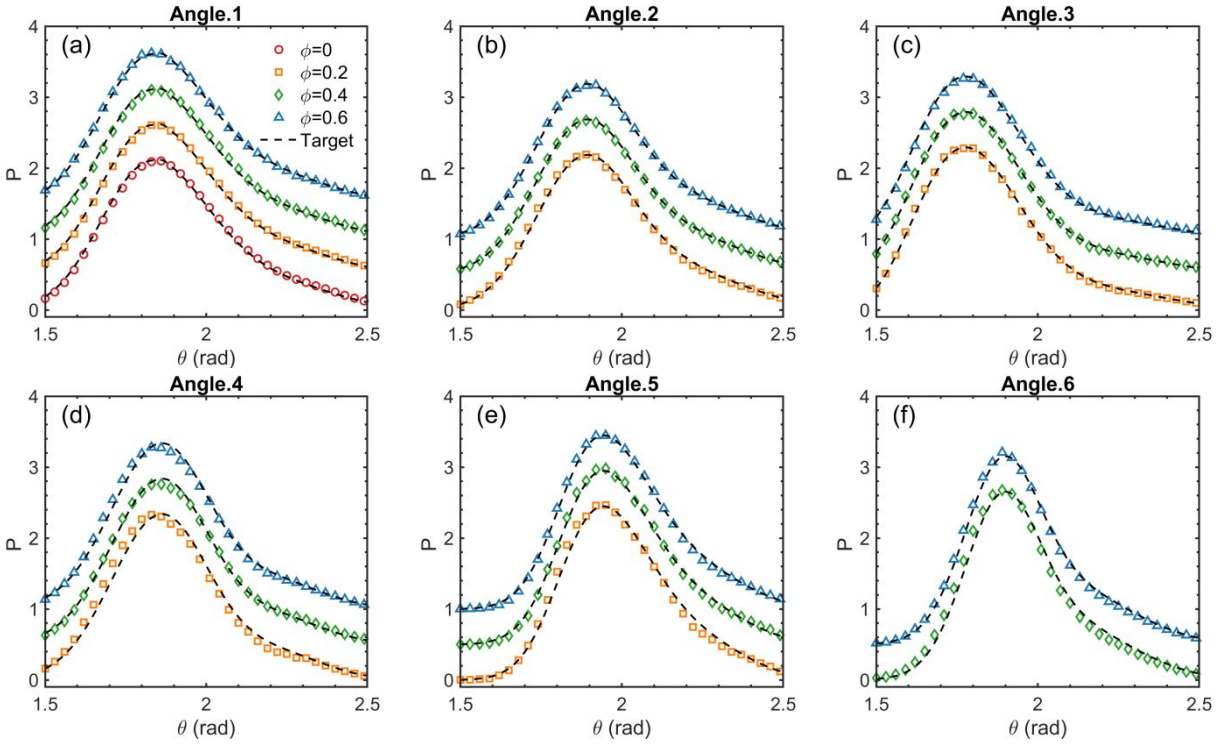

Figure 3. Angle distributions from simulations using the optimized CG model. (a) to (f) are for angle.1 to anlge.6, respectively. The dashed black lines are the AA target distribution, based on which CG potentials were optimized. Vertical shifts are applied for visual clarity. Shapes and locations of peak slightly differ for all distributions. The distributions cannot be fitted by single mode gaussian functions. Therefore, multimode gaussian functions were used to fit the distributions and then to derive CG angle potentials in tabulated form.

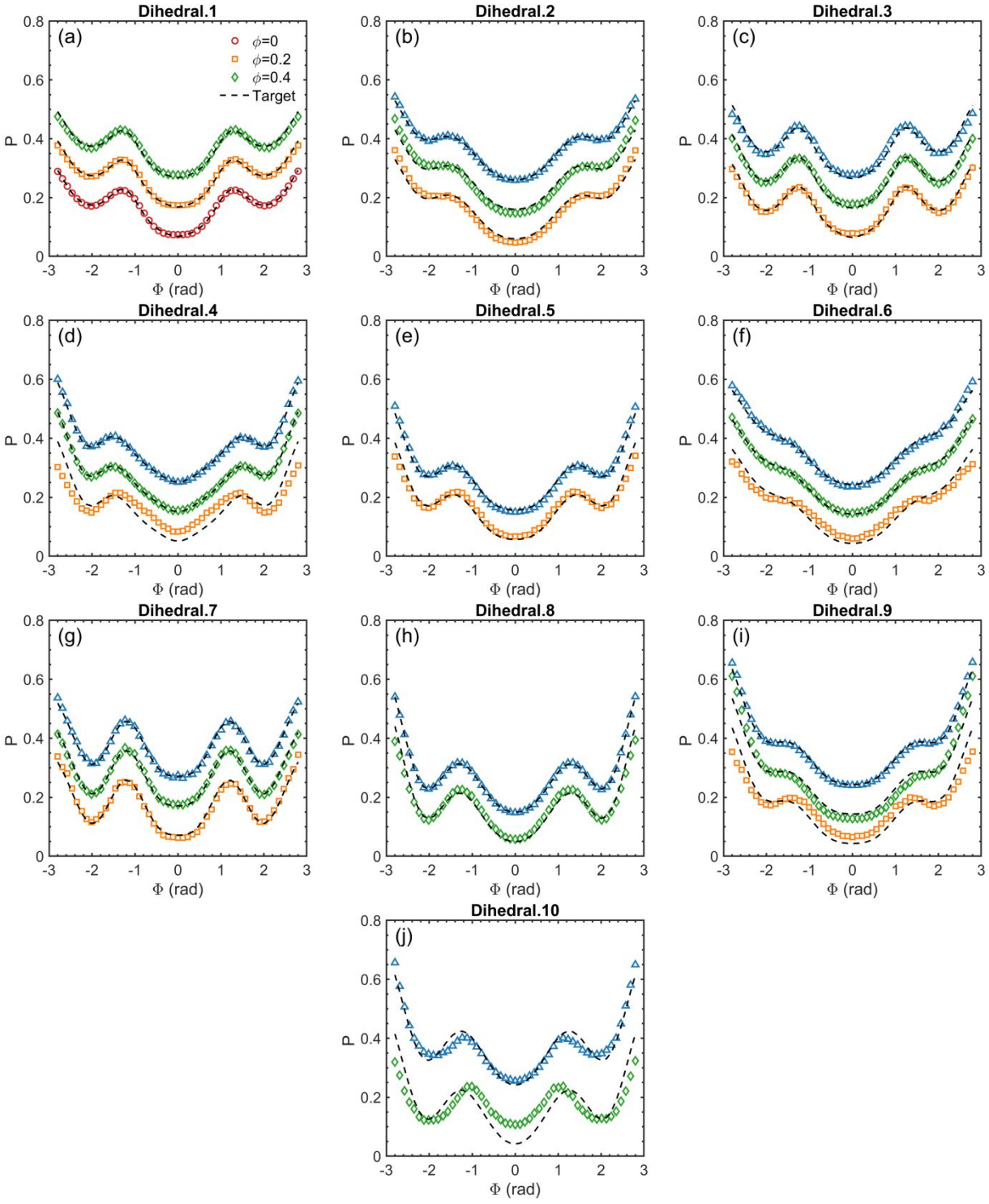

Figure 4. Dihedral distributions from simulations using the optimized CG model. The dashed black lines are the AA target distribution, based on which CG potentials were optimized. Vertical shifts are applied for visual clarity. Overall, the distributions are well captured by the CG model. Only minor deviations are shown in diherdar.4, diherdar.9, and diherdar.10, which are attributed to the limited statistics in these cases.

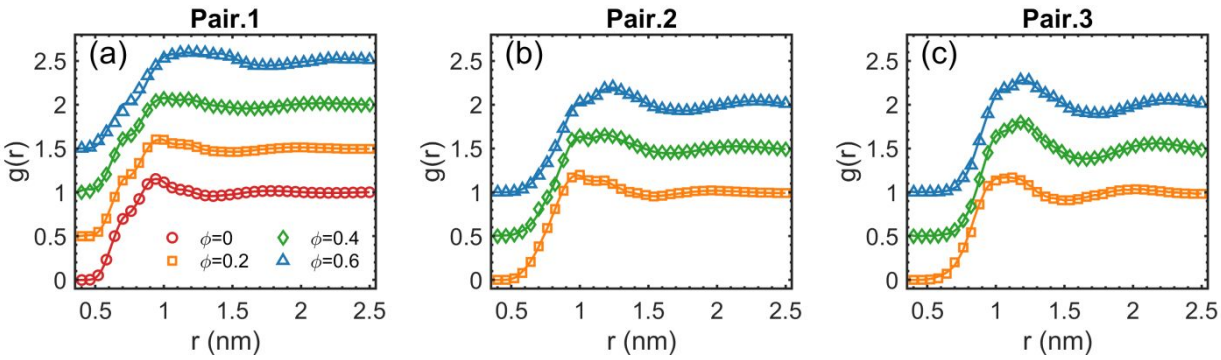

Figure 5. Pair distributions (or RDFs) from simulations using the optimized CG model. Unlike the distributions of bonded-interaction, the RDFs are ϕ-dependent. Solid lines are the AA target distributions while the symbols stand for corresponding CG results. Vertical shifts are applied for visual clarity.

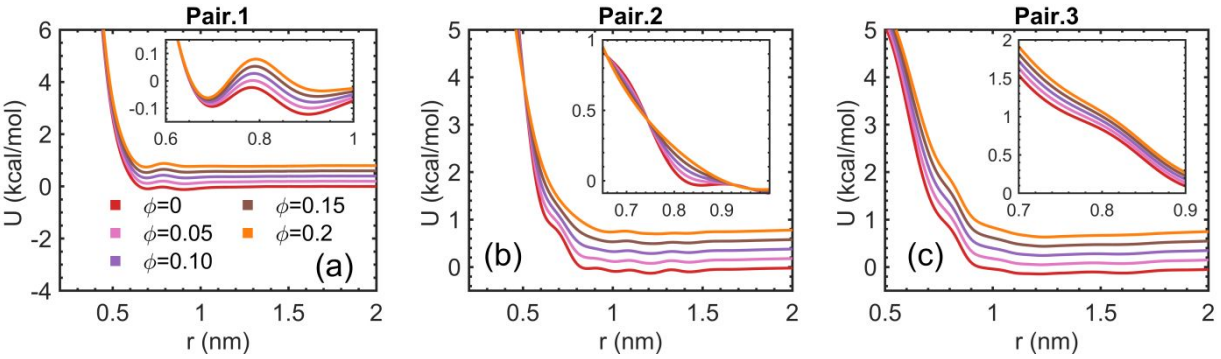

Figure 6. Interpolation of pairwise potentials by the lever rule (Eq. 3) for systems of ϕ=0.05, 0.1, 0.15. The potentials transit from ϕ=0 to 0.2 smoothly. Curves were shifted vertically on the main panels while no shift was applied to the insets. The IBI-optimized potentials for ϕ=0 and 0.2 are included for comparison. The elevations of the potentials dictate the increase of inter-bead separation as ϕ increases, as found in our previous work.[41]

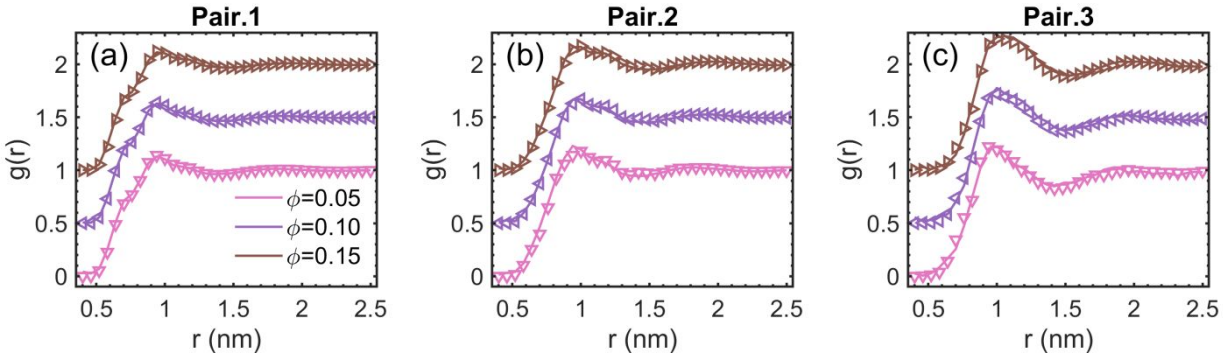

Figure 7. RDFs from simulations running with synthetic pair potentials for validation. Symbols and solid lines are CG results and AA ground truth respectively. Vertical shifts are applied for visual clarity. The structural characteristics are well captured by the CG model.

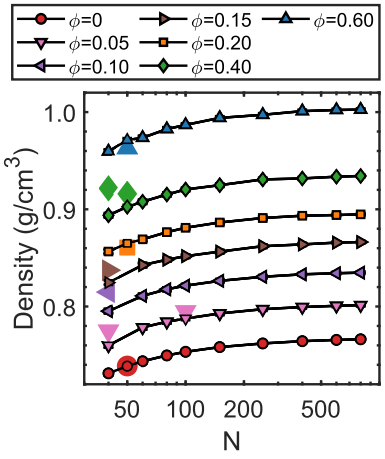

Figure 8. Density of all simulated systems at atmosphere pressure. Large unedged and small edged symbols are for AA and CG results respectively. Lines are guides to the eye. There is no pressure correction operation for ϕ=0.05, 0.1, and 0.15 systems. But the CG predicted values of density are consistent to the AA ground truth, surprisingly. Error bars stand for the standard deviation and their sizes are similar to the symbols.

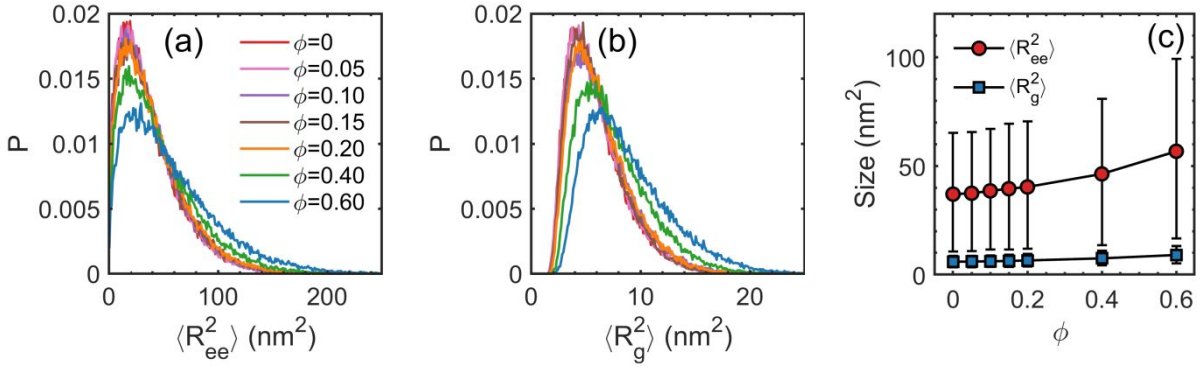

Figure 9. Characteristics of individual chains for N=100 with different values of ϕ. Distributions of mean-squared (a) end-to-end distance and (b) radius of gyrations change with the peaks shift rightward, as ϕ increases. The comparison in (c) shows that the copolymer molecules are in prolate ellipsoid shape, with aspect ratio increased as a function of ϕ. Error bars stand for standard deviations.

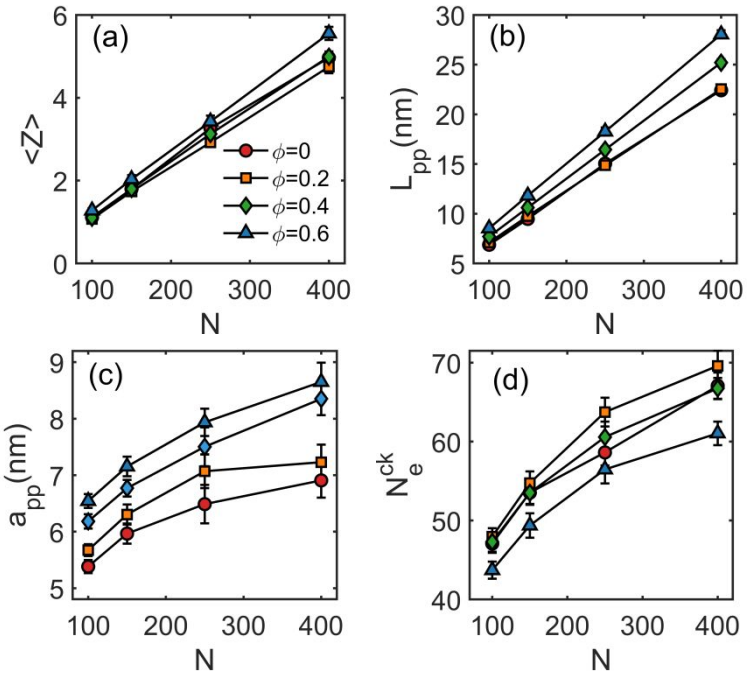

Figure 10. Structural characteristics of entangled chains change according to chain length N and ϕ. (a) average entanglement number per chain. (b) primitive path length. (c) tube diameter that quantifies the constraining strength of tube-like region. (d) average chain length between entanglement points. Results plotted as function of ϕ are provided in the Supplementary Information.

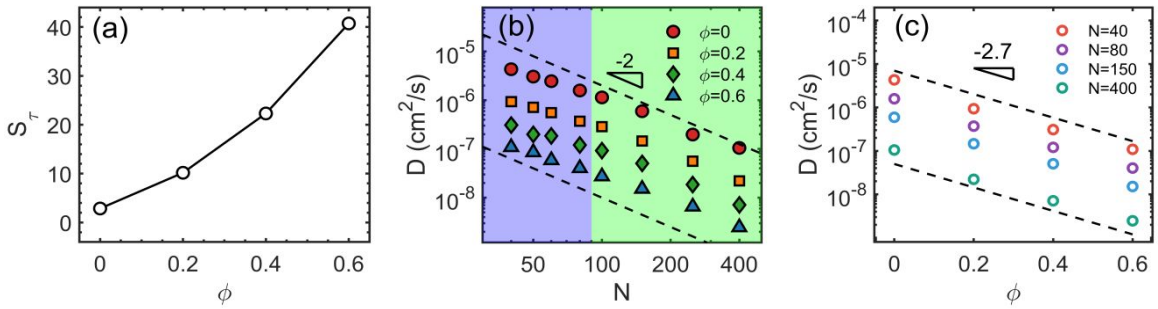

Figure 11. Dynamics of CG simulation systems. (a) time rescaling factor S_τ as a function of ϕ. (b) diffusion coefficient changes as N increases. Light blue and light green represent unentangled and entangled regions respectively. Power law according to the of Doi-Edwards tube model is indicated by the dashed line with slope of -2.0. The results suggest that N is too short to establish fully entangled systems in this work. (c) diffusion coefficient changes as ϕ increases. Dashed lines are the power law, with a -2.7 scaling, found in our previous AA simulation study.[41]

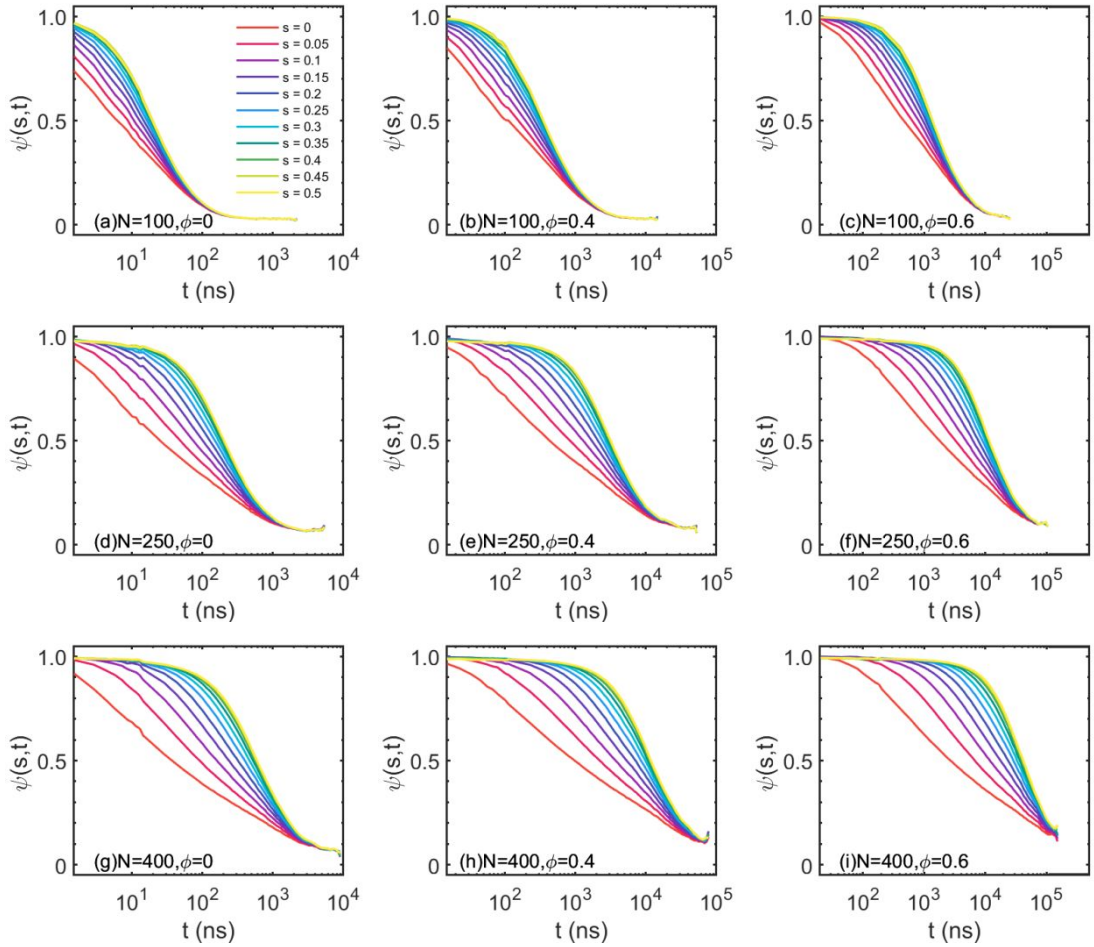

Figure 12. Tube survival probability that quantifies dynamics of the entangled systems. Full relaxation is indicated by the condition of ψ approaching to 0, suggesting that chains are fully out of the original tube. Relaxation time increases as N and ϕ increase.

References

1 S. C. Shit and P. Shah, *National academy science letters*, 2013, **36**, 355–365.

2 E. Yilgör and I. Yilgör, *Prog Polym Sci*, 2014, **39**, 1165–1195.

3 D. Campoccia, L. Montanaro and C. R. Arciola, *Biomaterials*, 2013, **34**, 8533–8554.

4 M. Razavi, R. Primavera, A. Vykunta and A. S. Thakor, *Materials Science and Engineering: C*, 2021, **119**, 111615.

5 C. Pang, C. Lee and K.-Y. Suh, *J Appl Polym Sci*, 2013, **130**, 1429–1441.

6 K. Raj M and S. Chakraborty, *J Appl Polym Sci*, 2020, **137**, 48958.

7 K.-H. Ha, H. Huh, Z. Li and N. Lu, *ACS Nano*, 2022, **16**, 3442–3448.

8 A. S. Palsule, S. J. Clarson and C. W. Widenhouse, *J Inorg Organomet Polym Mater*, 2008, **18**, 207–221.

9 A. Maiti, W. Small, M. P. Kroonblawd, J. P. Lewicki, N. Goldman, T. S. Wilson and A. P. Saab, *J Phys Chem B*, 2021, **125**, 10047–10057.

10 F. Wu, B. Chen, Y. Yan, Y. Chen and M. Pan, *Polymers (Basel)*, 2018, **10**, 522.

11 H. Chang, Z. Wan, X. Chen, J. Wan, L. Luo, H. Zhang, S. Shu and Z. Tu, *Appl Therm Eng*, 2016, **104**, 472–478.

12 K. Xiang, G. Huang, J. Zheng, X. Wang, G. xian Li and J. Huang, *Journal of Polymer Research*, 2012, **19**, 1–7.

13 U. Kumar, T. Kato and J. M. J. Frechet, *J Am Chem Soc*, 1992, **114**, 6630–6639.

14 R. Lund, A. Alegria, L. Goitandia, J. Colmenero, M. A. González and P. Lindner, *Macromolecules*, 2008, **41**, 1364–1376.

15 N. Bosq, N. Guigo, J. Persello and N. Sbirrazzuoli, *Physical Chemistry Chemical Physics*, 2014, **16**, 7830–7840.

16 T. Dollase, H. W. Spiess, M. Gottlieb and R. Yerushalmi-Rozen, *Europhys Lett*, 2002, **60**, 390.

17 W. Wang, W. Wang, F. Wang, X. Xie, G. Yi and Z. Li, *J Mater Chem A Mater*, 2022, **10**, 23375–23383.

18 C. A. Massa, S. Pizzanelli, V. Bercu, L. Pardi and D. Leporini, *Macromolecules*, 2017, **50**, 5061–5073.

19 V. Arrighi, S. Gagliardi, F. Ganazzoli, J. S. Higgins, G. Raffaini, J. Tanchawanich, J. Taylor and M. T. F. Telling, *Macromolecules*, 2018, **51**, 7209–7223.

20 P. Klonos, I. Y. Sulym, D. Sternik, P. Konstantinou, O. V Goncharuk, A. Deryło–Marczewska, V. M. Gun'ko, A. Kyritsis and P. Pissis, *Polymer (Guildf)*, 2018, **139**, 130–144.

21 B. T. Gall, R. Thomann and R. Mülhaupt, *J Polym Sci A Polym Chem*, 2011, **49**, 2339–2345.

22 K. Aissou, M. Mumtaz, G. Fleury, G. Portale, C. Navarro, E. Cloutet, C. Brochon, C. A. Ross and G. Hadziioannou, *Advanced materials*, 2015, **27**, 261–265.

23 S. Nagarajan and E. B. Gowd, *Macromolecules*, 2015, **48**, 5367–5377.

24 M. Brogly, S. Bistac, C. Delaite and C. Alzina, *Polym Int*, 2020, **69**, 1105–1112.

25 H. M. Li and J. H. Magill, *Polymer (Guildf)*, 1978, **19**, 829–836.

26 S. Wang and J. E. Mark, *J Mater Sci*, 1990, **25**, 65–68.

27 C. Chou and M.-H. Yang, *Journal of thermal analysis*, 1993, **40**, 657–667.

28 M.-H. Yang, W.-J. Huang, T.-C. Chien, C.-M. Chen, H.-Y. Chang, Y.-S. Chang and C. Chou, *Polymer (Guildf)*, 2001, **42**, 8841–8846.

29 A. Chien, R. S. Maxwell, S. DeTeresa, L. Thompson, R. Cohenour and B. Balazs, *J Polym Sci B Polym Phys*, 2006, **44**, 1898–1906.

30 A. Zlatanic, D. Radojcic, X. Wan, J. M. Messman and P. R. Dvornic, *Macromolecules*, 2017, **50**, 3532–3543.

31 A. Zlatanic, D. Radojcic, X. Wan, J. M. Messman, D. E. Bowen and P. R. Dvornic, *J Polym Sci A Polym Chem*, 2019, **57**, 1122–1129.

32 S. Morariu, C. E. Brunchi, M. Cazacu and M. Bercea, *J Chem Eng Data*, 2011, **56**, 1468–1475.

33 W. Xian, C.-H. Liu, B. Kangarlou, S.-Y. Chang, C. Wu, Y. Cao, L. Sun, A. W. K. Ma, M.-P. Nieh, A. Maiti and others, *ACS Appl Polym Mater*, 2023, **5**, 1915–1925.

34 C. Wu, J. Jin, X. Yang, H. Dong, X. Xu and J. Jiang, *J Appl Polym Sci*, 2010, **117**, 2530–2537.

35 S. Xu, L. Xie, X. Yu, Y. Xiong and H. Tang, *J Polym Sci A Polym Chem*, 2015, **53**, 1794–1805.

36 L. Qu, Z. Xie, G. Huang and Z. Tang, *J Polym Sci B Polym Phys*, 2008, **46**, 1652–1659.

37 L. Zhu, X. Cheng, W. Su, J. Zhao and C. Zhou, *Polymers (Basel)*, 2019, **11**, 1989.

38 S. M. M. Alam, A. H. Ashik and A. K. M. N. Ul-Hossain, *Mater Today Proc*, 2022, **54**, 951–957.

39 W. G. Noid, *J Phys Chem B*, 2023, **127**, 4174–4207.

40 T. E. Gartner III and A. Jayaraman, *Macromolecules*, 2019, **52**, 755–786.

41 W. Xian, J. He, A. Maiti, A. P. Saab and Y. Li, *Soft Matter*, 2023, **19**, 4265–4276.

42 A. Karatrantos, N. Clarke and M. Kröger, *Polymer reviews*, 2016, **56**, 385–428.

43 Y. Li, B. C. Abberton, M. Kröger and W. K. Liu, *Polymers (Basel)*, 2013, **5**, 751–832.

44 H. Ye, W. Xian and Y. Li, *ACS Omega*, 2021, **6**, 1758–1772.

45 Y. Li, S. Tang, B. C. Abberton, M. Kröger, C. Burkhart, B. Jiang, G. J. Papakonstantopoulos, M. Poldneff and W. K. Liu, *Polymer (Guildf)*, 2012, **53**, 5935–5952.

46 V. A. Harmandaris and K. Kremer, *Macromolecules*, 2009, **42**, 791–802.

47 A. P. Thompson, H. M. Aktulga, R. Berger, D. S. Bolintineanu, W. M. Brown, P. S. Crozier, P. J. In't Veld, A. Kohlmeyer, S. G. Moore, T. D. Nguyen and others, *Comput Phys Commun*, 2022, **271**, 108171.

48 W. Humphrey, A. Dalke and K. Schulten, *J Mol Graph*, 1996, **14**, 33–38.

49 D. Zhang, Y. Wang, M. Safaripour, D. A. Bellido-Aguilar, K. R. Van Donselaar, D. C. Webster, A. B. Croll and W. Xia, *Physical Chemistry Chemical Physics*, 2024, **26**, 4541–4554.

50 V. Ruhle, C. Junghans, A. Lukyanov, K. Kremer and D. Andrienko, *J Chem Theory Comput*, 2009, **5**, 3211–3223.

51 S. Shanbhag and M. Kröger, *Macromolecules*, 2007, **40**, 2897–2903.

52 N. C. Karayiannis and M. Kröger, *Int J Mol Sci*, 2009, **10**, 5054–5089.

53 M. Kröger, J. D. Dietz, R. S. Hoy and C. Luap, *Comput Phys Commun*, 2023, **283**, 108567.

54 P.-G. De Gennes, *J Chem Phys*, 1971, **55**, 572–579.

55 M. Doi, S. F. Edwards and S. F. Edwards, *The theory of polymer dynamics*, oxford university press, 1988, vol. 73.

56 J. D. Dietz, M. Kroger and R. S. Hoy, *Macromolecules*, 2022, **55**, 3613–3626.

57 P. S. Stephanou, C. Baig, G. Tsolou, V. G. Mavrantzas and M. Kröger, *J Chem Phys*.

58 P. S. Stephanou, C. Baig and V. G. Mavrantzas, *Soft Matter*, 2011, **7**, 380–395.

59 R. Auhl, R. Everaers, G. S. Grest, K. Kremer and S. J. Plimpton, *J Chem Phys*, 2003, **119**, 12718–12728.

60 J. T. Padding and W. J. Briels, *J Chem Phys*, 2002, **117**, 925–943.

61 L. J. Fetters, D. J. Lohse, D. Richter, T. A. Witten and A. Zirkel, *Macromolecules*, 1994, **27**, 4639–4647.

62 R. Everaers, *Physical Review E—Statistical, Nonlinear, and Soft Matter Physics*, 2012, **86**, 22801.

63 R. S. Hoy, K. Foteinopoulou and M. Kröger, *Physical Review E—Statistical, Nonlinear, and Soft Matter Physics*, 2009, **80**, 31803.

64 B. R. Harkness, M. Tachikawa, H. Yue and I. Mita, *Chemistry of materials*, 1998, **10**, 1700–1705.

65 *Annual Review of Materials Science*, 1996, **26**, 501–550.

66 G. Zhang, J. Steck, J. Kim, C. H. Ahn and Z. Suo, *Sci Adv*, 2023, **9**, eadh7742.

67 Z. Chen, G. Zhang, Y. Luo and Z. Suo, *Proceedings of the National Academy of Sciences*, 2024, **121**, e2322684121.

68 L. Qu, G. Huang, Q. Wang and Z. Xie, *J Polym Sci B Polym Phys*, 2008, **46**, 72–79.

69 T. M. Gädda and W. P. Weber, *J Polym Sci A Polym Chem*, 2006, **44**, 3629–3639.

70 Y. Wang, Z. Li, K. Niu and W. Xia, *Polymer (Guildf)*, 2022, **256**, 125159.

71 X.-Z. Zhang, Z.-Y. Lu and H.-J. Qian, *Macromolecules*, 2023, **56**, 3739–3753.

72 J.-F. Lutz, M. Ouchi, D. R. Liu and M. Sawamoto, *Science (1979)*, 2013, **341**, 1238149.

73 C. Yang, K. B. Wu, Y. Deng, J. Yuan and J. Niu, *ACS Macro Lett*, 2021, **10**, 243–257.

74 G. Chen, Z. Shen, A. Iyer, U. F. Ghumman, S. Tang, J. Bi, W. Chen and Y. Li, *Polymers (Basel)*, 2020, **12**, 163.

75 L. Tao, J. Byrnes, V. Varshney and Y. Li, *iScience*.

All data needed to evaluate the conclusions in the paper are present in the paper and/or the Supplementary Materials.